Research Article | Vol. 27, No. 19 / 16 September 2019 / Optics Express 26728

Optics EXPRESS

Direct observation of multimode interference in rare-earth doped micro/nanofibers

Bigeng Chen,[1,2,3] Qingyang Bao,[1] and Limin Tong[1,*]

[1] *State Key Laboratory of Modern Optical Instrumentation, College of Optical Science and Engineering, Zhejiang University, Hangzhou 310027, China*

[2] *B. Chen is now with Optoelectronics Research Centre in University of Southampton, Southampton SO17 1BJ, UK*

[3] *bigeng.chen@soton.ac.uk*

[*] *phytong@zju.edu.cn*

Abstract: Modal inspection of optical fibers is important for multimode application but it is challenging to collect in-situ information of propagating modes for evaluation and manipulation. Here we demonstrate direct observation of multimode interference in Er^{3+}/Yb^{3+} co-doped micro/nanofibers. Luminescent interference patterns are visualized by visible up-conversion of Er^{3+} ions and are used for establishing the existence of higher order modes co-propagating with fundamental modes. We use fast Fourier transform to analyze the patterns in detail and obtain excellent agreement between experiment and calculation on beat lengths of the interference. Effective index differences among higher order modes and a fundamental mode of a microfiber are also experimentally investigated with the assistance of interference patterns, revealing the characteristic of modal dispersions.

1. Introduction

As mature optical gain mediums, rare-earth doped glass optical fibers have found numerous applications in lasers [1,2], amplifiers [3,4] and sensors [5,6]. Similar to the state-of-art optical fibers fabricated from bulk preforms [7], active micro/nanofibers can also be directly drawn from rare-earth doped bulk glasses [8], which provide various advantages such as strong optical confinement, high optical intensity and compact size [9]. Previous studies had demonstrated multiple miniature fiber lasers using rare-earth doped microfibers [10–12]. On the other hand, higher order transverse modes with more complex modal properties offer additional dimension of freedom to manipulate optical field for various applications, and thus have attracted wide interest on relevant topics ranging from propagation characteristics [13,14], selective mode excitation/conversion [15,16] to particle trapping [17,18], higher order mode lasers [19,20], optical vortex generation [21,22] and so on. To inspect fiber modes, one common method is direct imaging of modal profiles at a fiber's output end. In this way polarizers are needed to distinguish some higher order modes with similar intensity profiles [20]. It is also challenging to study mode evolution along propagation. Another approaches are to detect optical field from fiber or waveguide surfaces by using near-field scanning optical microscopy (NSOM) or Rayleigh scattering [23–25]. However, NSOM is limited by its operation complexity and possible damage to samples. Also Rayleigh scattering is rather weak for signal collection from geometrically uniform fibers (the corresponding loss is less than 1 dB/km for near infrared wavelength [26]).

Here we report that, direct observation of multimode interference in a fiber and subsequent mode resolving are feasible based on the platform of rare-earth doped micro/nanofibers. When excited by continuous wave (CW) laser light at 976 nm with power as small as 10 μW, our Er^{3+}/Yb^{3+} co-doped tellurite glass micro/nanofibers showed distinct multimode interference patterns on their surfaces owing to the strong up-conversion luminescence. Fundamental and higher order modes were then resolved from fast Fourier transform (FFT) results of the patterns

#370997 https://doi.org/10.1364/OE.27.026728
Journal © 2019 Received 27 Jun 2019; revised 13 Aug 2019; accepted 15 Aug 2019; published 9 Sep 2019

Optics EXPRESS

in combination with optical mode calculation. We obtained a remarkable agreement between experiment and calculation. Only a few tens of micrometers in length of a doped nanofiber is needed to extract multimode interference information. Using this approach, we also investigated experimentally the trend of effective index differences between higher order modes and a fundamental mode against wavelength at telecom range in a microfiber, indicating how the modal dispersions differ from each other.

2. Fabrication and up-conversion luminescence of Er^{3+}/Yb^{3+} co-doped tellurite glass fibers

The doped tellurite glass micro/nanofibers were fabricated by the method described in [8]. Firstly, we took a little portion from a locally melt bulk glass (0.5 mol% of Er^{3+} and 2 mol% of Yb^{3+}) by a heated sapphire rod. Then another sapphire fiber was used to draw micro/nanofibers from that fused portion adhesive on the rod. Figure 1(a) gives a scanning electron microscopy (SEM) image of a 780-nm-diameter fiber, which exhibits excellent uniformity and smooth surface. We used a 976-nm CW laser to excite a doped microfiber and collect the luminescence spectrum from visible to near infrared regime with an evanescent coupling scheme [8]. Two tapered fiber probes were used to attach the two ends of the microfiber for input and output couplings. The laser light was sent into the input fiber probe to excite the microfiber and the photoluminescence was collected by a spectroscope (Yokogawa AQ6315) via the output fiber probe. The measured spectrum in Fig. 1(b) contains many transition emissions of Er^{3+} and Yb^{3+} including two up-conversion transitions around 550 nm and 665 nm dominating in the visible regime (red dashed frame), which were contributed by transitions from excited states $^4S_{3/2}$, $^4F_{9/2}$ to ground state $^4I_{15/2}$ of Er^{3+}, respectively [27]. During the up-conversion process, energy of electrons at $^2F_{5/2}$ of Yb^{3+} was transferred efficiently to those at the excited state $^4I_{11/2}$ of Er^{3+}, populating them to the higher states where the radiative transitions occurred with visible emissions.

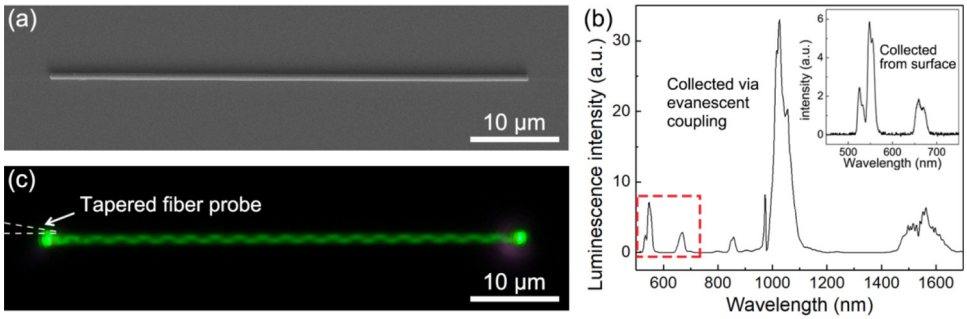

Fig. 1. SEM image and up-conversion luminescence of Er^{3+} doped tellurite glass micro/nanofibers. (a) SEM image of a 780-nm-diameter nanofiber. (b) Photoluminescence spectrum of a doped microfiber covering a wide spectral range. Inset: visible up-conversion spectrum collected from the surface of the nanofiber in Fig. 1(a). (c) Periodic luminescent pattern on the nanofiber. The dashed lines indicate the fiber probe for excitation.

Next we excited the 780-nm-diameter fiber in Fig. 1(a) by the same laser with horizontal polarization through a silica tapered fiber probe. The nanofiber was supported on an MgF_2 substrate under an optical microscope (Nikon Ci-S) with two 10x eyepieces and a 100x objective (1000x magnification). Without illumination, we observed a distinct periodic zigzag pattern on the nanofiber (Fig. 1(c)) collected by a CCD (Nikon DS-Fi1c, resolution 2560×1920) attached in the microscope. The laser power output from the tapered fiber probe was about 10 μW and the CCD exposure time was 0.1 second. Actually, the luminescence was so bright that it was seen by naked eyes. In the inset of Fig. 1(b) the spectrum collected from the surface of the excited

Optics EXPRESS

nanofiber confirmed that the luminescent zigzag pattern came from up-conversion of Er^{3+}. With higher spectral resolution, the emission at around 525 nm was also resolved, which was induced by the transition from $^2H_{11/2}$ to $^4I_{15/2}$ of Er^{3+} [27].

3. Analysis of multimode interferences in rare-earth doped micro/nanofibers

To study the photoluminescence pattern, we extracted the CCD image intensity along the dashed line in Fig. 2(a) (enlarged image of the middle area in Fig. 1(c)) and obtained a typical 1D profile given in Fig. 2(b), from which strong oscillation and small envelope ripple can be observed. To fully explore the spatial frequency information of the luminescence pattern we performed FFT on each 1D horizontal pixel array with intensity profile and plotted a 2D FFT spectral graph dependent on position along vertical direction (marked as x) in Fig. 2(a), as shown in upper part of Fig. 2(c). The pixel size in the captured luminescence image corresponds to about 0.046 μm in length, calculated by averaging a long measured distance over its accumulated pixels along one dimension. Since FFT frequency resolution equals sampling frequency divided by the length of sampled discrete signal (989 points), the obtained frequency resolution is 0.022 μm^{-1}. We believe the limited resolution was the dominating error source in the experiment. Hence it is used as the error range of the measured frequency. The 1D FFT spectrum along the dashed line is given in lower part of Fig. 2(c) to reflect all existing peaks. From the FFT spectrum three evident peaks are spotted at 0.373 ± 0.022 μm^{-1}, 0.329 ± 0.022 μm^{-1} and 0.225 ± 0.022 μm^{-1}.

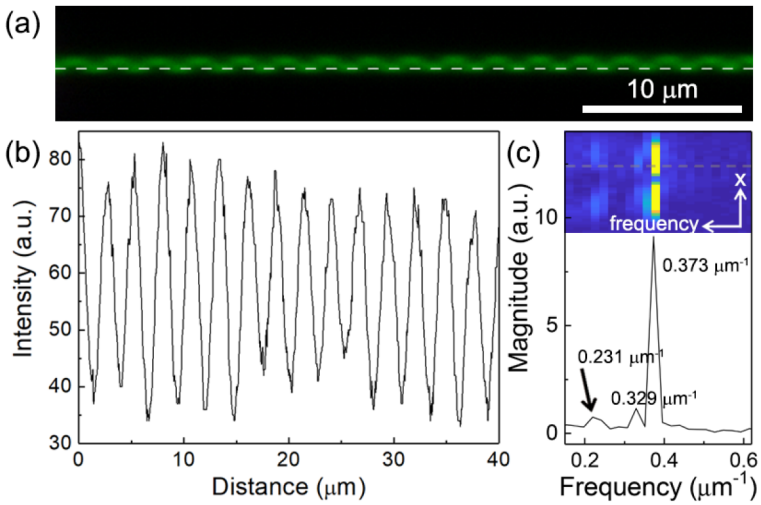

Fig. 2. Photoluminescence and spatial frequency information of the nanofiber with horizontally-polarized input. (a) Enlarged view of the middle area in Fig. 1(c). (b) Extracted luminescence intensity profile along the dashed line in Fig. 2(a). (c) Upper: 2D FFT spectral graph dependent on x position transformed from Fig. 2(a); Lower: 1D FFT spectrum along the dashed line in the upper part.

The periodic pattern is believed owing to multimode interference within the nanofiber. To construct an intuitive picture of the interference, firstly we used COMSOL to calculate the optical modes supported by the 780-nm-diameter nanofiber. The refractive indices of tellurite glass and MgF_2 used in calculation are 2 and 1.38, respectively, corresponding to a V number of 4.349 for 976 nm wavelength. We think that a fundamental mode with the same polarization as the excitation is very likely to be excited instead of its orthogonal counterpart, which is supported by our simulation of evanescent coupling between a tapered fiber and a cylindrical fiber in Lumerical FDTD. Because the input was horizontally polarized in our experiment, we start from

Optics EXPRESS

the horizontal component of the calculated modal field distributions. As shown in Figs. 3(a) and 3(b), the electric field for fundamental HE_{11-x} mode is horizontally symmetric while the one for TM_{01} mode is anti-symmetric. Because of their different effective indices, co-propagating of these two modes will produce beats along the propagation direction due to periodic constructive and destructive interferences, which had contributed to the observed strong oscillation. The beat length can be expressed by [25]

$$L = \frac{\lambda}{|n_1 - n_2|}. \tag{1}$$

L is the beat length, λ is the wavelength in vacuum, n_1 and n_2 are the mode effective indices. As the calculated effective indices of HE_{11-x} and TM_{01} modes for the nanofiber at 976 nm wavelength are 1.813 and 1.456, respectively, the beat length of these two modes is 2.737 μm theoretically. This value agrees well with the experiment result of 2.681 ± 0.159 μm obtained by taking reciprocal of the peak position 0.373 ± 0.022 μm^{-1} in the FFT spectrum. Similarly, the peak at 0.231 ± 0.022 μm^{-1} corresponding to a beat length of 4.329 ± 0.416 μm can be assigned to the interference of HE_{11-x} and TE_{01} modes with a theoretical value of 4.440 μm, and 0.329 ± 0.022 μm^{-1} (reciprocal 3.040 ± 0.204 μm) for the interference of HE_{21-odd} and HE_{11-x} modes (beat length 2.942 μm in theory). In Fig. 3(c) the horizontal electric field of TE_{01} mode shows a near anti-symmetric distribution along vertical direction, suggesting the reason for the envelope ripple in the luminescence. HE_{21-odd} mode also has a similar horizontal electric field to that of TE_{01} mode. We used Lumerical FDTD to simulate the HE_{11-x} and TM_{01} modes propagating in the nanofiber simultaneously to reproduce the most pronounced pattern. The magnitude distribution of Poynting vectors on the xz plane across the fiber axis (denoted by the red dashed frame in Fig. 3(d)) is given in Fig. 3(e), showing a periodic pattern nearly the same as that in Fig. 1(c). These results confirm that multimode interference was the reason for the observed luminescent pattern on the nanofiber and was visualized by the visible part of Er^{3+} ions up-conversion. We consider that the tiny silica fiber probe (tip diameter less than 100 nm) used for input had facilitated the excitation of higher order modes because the input mode index is smaller than the fundamental mode index of the thicker micro/nanofibers.

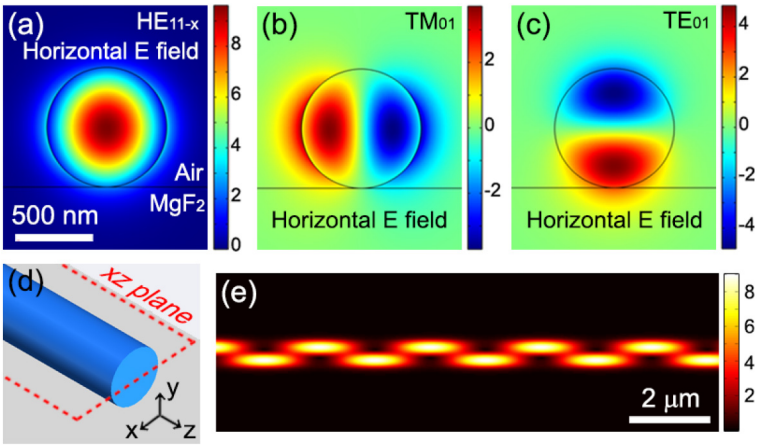

Fig. 3. Numerical simulation of the nanofiber. (a-c) Calculated transverse distributions of horizontal electric field for HE_{11-x}, TM_{01} and TE_{01} modes, respectively, in a 780-nm-diameter nanofiber. The subscript "x" is used as a denotation of horizontal polarization. (d) Geometrical model of a nanofiber in Cartesian coordinates. (e) Simulated magnitude distribution of Poynting vectors on the xz plane across the fiber axis (denoted by the red dashed frame in Fig. 3(d)) when HE_{11-x} and TM_{01} modes are launched simultaneously into the nanofiber.

Optics EXPRESS

Compared with the strong interference between horizontal components (along x) of different modes, the interference between vertical components (along y) was relatively weak, which can be explained with two main reasons. Firstly very little amount of x-polarized input light was coupled to HE_{11-y} mode with the orthogonal polarization, hence interference between HE_{11-y} mode and higher order modes can be regarded as negligible. Secondly the overlapping of the vertical components of TM_{01} and TE_{01} (HE_{21-odd}) modes was rather limited and the power fraction of TE_{01} and HE_{21-odd} modes were very small. Therefore, interference between higher order modes didn't contribute much either. To quantify the overlapping we calculated spatial cross correlation with different modal fields. All the calculated modes had the same amplitude of 1 V/m set in Lumerical FDTD and absolute values of field were taken for correlation. As a result, the maximum cross correlation (when the circular fiber cross sections are completely overlapped in space) for the vertical components of TM_{01} and TE_{01} modal fields, for example, is about 46 V^2/m^2, which is only 14% of that for the horizontal components of TM_{01} and HE_{11-x} modal fields (320 V^2/m^2). Due to the presence of the substrate, most vertical component of TM_{01} mode is outside the nanofiber, especially in the two gaps on left and right sides formed by the nanofiber and the substrate depicted in Fig. 4(a). However, the fiber still confines the vertical component of TE_{01} mode tightly, as shown in Fig. 4(b). When the absolute field amplitude of the vertical component is integrated over the transverse surface, it turns out that 67% of the field is inside the fiber for TE_{01} mode while only 22% for TM_{01} mode. These confinement results also explain the weak overlapping of vertical field between TM_{01} and TE_{01} modes. We noted that if the nanofiber was air-cladded it would also support HE_{31} and EH_{11} modes but the presence of the substrate had led to the cutoff of these modes. At the same time HE_{11} and HE_{21} mode became non-degenerated. As a result, the number of supported modes remains the same which is 6 in total.

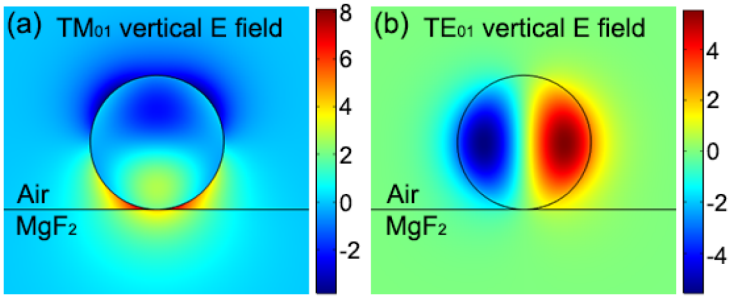

Fig. 4. Vertical electric field components of TM_{01} mode (a) and TE_{01} mode (b) of the same fiber in Fig. 3(a).

With the same coupling scheme, we also used vertically polarized input light to excite the doped nanofiber for further investigation of multimode interference. A different luminescent pattern was observed as shown in Fig. 5(a). Employing the abovementioned method, we obtained three peaks at 0.114 ± 0.022 μm^{-1}, 0.228 ± 0.022 μm^{-1} and 0.354 ± 0.022 μm^{-1} in the FFT spectrum given in Fig. 5(b), corresponding to beat lengths of 8.772 ± 2.048 μm, 4.386 ± 0.457 μm and 2.825 ± 0.203 μm, respectively. The horizontal cutline for frequency domain analysis was taken around the position where the periodicity was most significant on the luminescence image. Compared with the beat lengths of all possible multimode interferences supported in the nanofiber, the experimental results are successfully matched with those of the interferences of HE_{21-odd} - TE_{01}, HE_{11-y} - TE_{01} and HE_{21-odd} - HE_{11-y}, which have theoretical beat lengths of 8.707 μm, 4.388 μm and 2.918 μm, respectively. The experiment and calculation show a remarkable agreement. We noted that because the central symmetry in the fiber cross section is broken by the substrate, the two degenerated HE_{21} modes became non-degenerated with different modal properties. The HE_{21-odd} mode involved in our observation is less distorted

Optics EXPRESS

by the substrate than its counterpart $HE_{21-even}$ whose field is mainly (>90%) along the vertical direction. Similar to Fig. 2(c), we plot the 2D FFT spectral graph dependent on x position as shown in the inset of Fig. 5(b). As the frequency axis aligns with that of the main figure, the graph depicts that the peak positions generally remain the same regardless of x position. Two of the peaks vanish in the middle as the periodicity is much less significant along the nanofiber's middle line. We also see that owing to diffraction limitation of the optical microscope, the spatial range of the captured luminescence along x direction is quite beyond the edge positions of the nanofiber along x marked by the gray dashed lines.

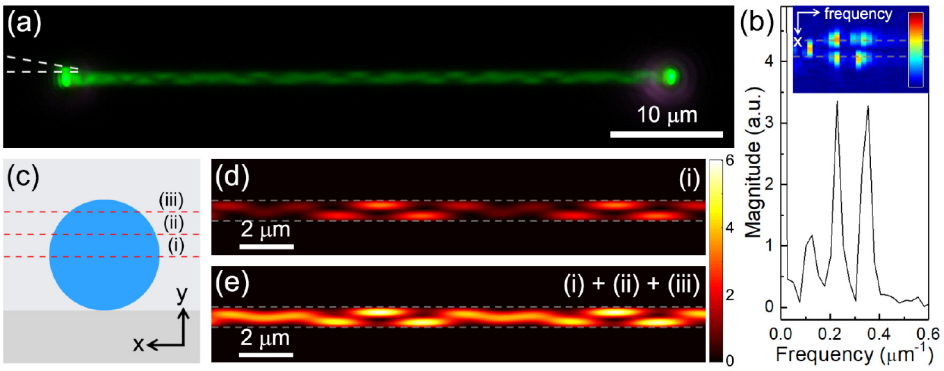

Fig. 5. Multimode interference with vertically-polarized input. (a) Luminescence pattern on the nanofiber with TM-polarized excitation. The dashed lines indicate the position of launching fiber taper tip. (b) FFT spectrum of a 1D luminescent intensity profile extracted from Fig. 5(a). Inset: 2D FFT spectral graph dependent on x position. The gray dashed lines mark the edge positions along x of the nanofiber. (c) Cross-section view of a substrate-supported nanofiber model. (d) Simulated magnitude distribution of Poynting vectors on plane (i) as the HE_{11-y}, the TE_{01} and the HE_{21} modes are launched simultaneously into a 780-nm-diameter nanofiber. (e) Summation of the Poynting vector magnitude distributions on plane (i), (ii) and (iii). The gray dashed lines in Figs. 5(d) and 5(e) mark the nanofiber edges.

For better demonstration, we simulated these three modes propagating simultaneously in a 780-nm-diameter nanofiber by Lumerical FDTD. Fig. 5(d) gives the magnitude distribution of Poynting vectors on the xz plane across the fiber axis (plane (i) in Fig. 5(c)), showing a little similarity to the experiment observation in Fig. 5(a). Since up-conversions occurred not only in a single horizontal plane but everywhere with excited Er^{3+} ions in the nanofiber, we simply summed up the calculated magnitudes of plane (i), (ii) and (iii) (separated by 130 nm vertically, denoted in Fig. 5(c)) and obtained a superimposed distribution given in Fig. 5(e) with much better agreement with Fig. 5(a). This finding further verifies the three-mode interference in the nanofiber. We understand that the luminescent interference pattern isn't the result of a simple linear superposition. How the up-conversion photons propagated inside and escaped from the nanofiber were also involved in real experiment. Nonetheless our observation still captured most of the interference pattern feature, suggesting that to some extent the up-conversion photon distribution followed the interference field inside the nanofiber even when they were radiated out to far field.

4. Multimode interference dependent on wavelength at telecom range

Except the 976-nm laser, we also used a tunable laser at 1.5 μm telecom wavelength to excite the rare-earth doped fibers and once again observed multimode interference pattern with visible up-conversion. Due to the smaller excitation photon energy, multi-photon absorption occurred

Optics EXPRESS

in both Er^{3+} and Yb^{3+} to populate their excited states and realize a similar up-conversion involving energy transfer and excited state absorption mentioned above [28,29]. Although this up-conversion was considerably weaker, with 5-mW input power we easily captured a distinct interference pattern on a 1.18-μm-diameter doped microfiber as shown in Fig. 6(a). The V number of the microfiber is about 3.932 for 1550 nm while the change of supported modes owing to the presence of the substrate is same as the nanofiber mentioned above. Using different excitation wavelengths ranging from 1480 nm to 1580 nm under horizontal polarization, we obtained a series of FFT spectra extracted from the luminescent patterns, as depicted in Fig. 6(b). Interferences of HE_{11-x} mode with TE_{01} and TM_{01} modes were then resolved with the same approach. We derived the index differences from beat lengths based on Eq. (1) to compare with the calculation for different wavelengths (Fig. 6(c)). Material dispersion was assumed negligible within the wavelength range in our calculation as waveguide dispersion dominated due to the high refractive index contrast.

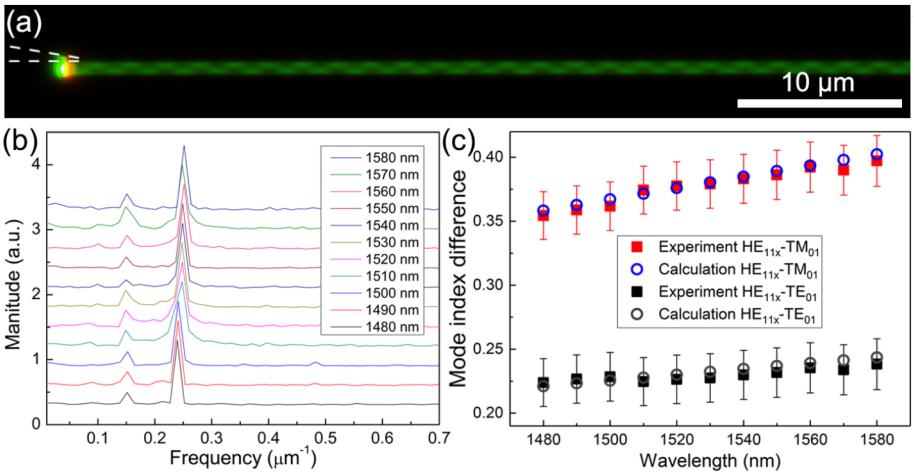

Fig. 6. (a) Luminescence pattern on a 1.18-μm-diameter nanofiber under 1480-nm TE-polarized excitation. (b) Extracted spatial frequency profiles from Luminescence beat patterns produced by excitations at different wavelengths. (c) Calculated and measured mode index difference of HE_{11-x} - TM_{01} and HE_{11-x} - TE_{01} dependent on wavelength. The range of the error bar is about ± 0.019.

In addition to the good agreement between the experiment and the calculation, Fig. 6(c) reveals an evident incremental trends of the effective mode index differences dependent on wavelength. We also noted a larger gradient of the HE_{11-x}-TM_{01} index difference than the other one. Combining the fact that all the three modes have negative dispersions, we can thus deduce that TM_{01} mode has the largest absolute dispersion while HE_{11-x} mode has the smallest one. At the same time their effective indices have an opposite order, i.e., $n_{HE11} > n_{TE01} > n_{TM01}$. The order of dispersions can be understood from the different fractions of evanescent field for different modes [30]. As we know generally higher order modes are less confined than fundamental modes, especially in the situation of high refractive index contrast and subwavelength waveguiding. For example, 18% of TM_{01} modal field is outside the microfiber and for TE_{01} mode this percentage is 15.6% while for HE_{11-x} mode it is only 3.6%. When more field spreads into the air cladding from the microfiber, the group velocity increases because of lower refractive index of the air [30], leading to the decrease of effective index. On the other hand, higher order modes are closer to mode cutoff criteria, near where the fraction of evanescent field in the cladding changes rapidly. Therefore, we expect larger dispersion for modes with stronger evanescent field and lower effective index just as the higher order modes we observed here. Because optical communication at C band

Optics EXPRESS

and L band is heavily dependent on rare-earth doped fibers for optical sources and amplifiers in fiber-based systems, direct observation of multimode interference at these wavelength regimes would be attractive for communication application as it could pace towards quantitative analysis and manipulation of optical modes in real time.

5. Discussion

In summary, we demonstrate the direct observation of multimode interferences in the Er^{3+}/Yb^{3+} co-doped tellurite glass micro/nano fibers via strong visible up-conversions of Er^{3+} ions. Clear images of the luminescent patterns can be easily captured with modest excitation laser power and CCD exposure time. We carried out FFT on spatial intensity distributions of the observed periodic patterns and obtained corresponding beat lengths of the interferences. Higher order modes propagating in the fibers were then resolved with the aid of numerical calculation. The experiment results agree with the calculation remarkably. Detailed comparison and analysis have been performed to explain the pronounced difference of multimode interferences with perpendicular excitation polarizations. We also present evolution of mode index difference dependent on wavelength at telecom range, revealing the dispersive characteristic difference between fundamental mode and higher order modes. This approach has enabled infrared propagating light detection with visible imaging system.

Beyond what have been shown in our study, one can readily use lower magnification imaging to inspect the interferences with much longer beat lengths. In this case exposure can be faster because more luminescence can be collected and each pixel receives more photons per unit time. Meanwhile, as long as the CCD resolution representing the spatial sampling frequency meets Nyquist sampling criterion (twice of signal frequency [31]), short beat lengths can still be recovered. This can be an advantage for weakly guiding fibers where effective indices are close in one modal family but quite different between different families [13,14]. Combining high and low magnification is another efficient way to inspect various beat lengths. In the condition that input polarization is not known, a polarizer can be placed at fiber output to assist polarization detection. Therefore, it also helps distinguishing modes with very close indices but different polarization as a strong supplementary method for the FFT analysis. Quantitative analysis of power fraction for different modes is also possible once we establish the corresponding relation between measured FFT amplitude and calibrated input of an arbitrary mode. Adding luminescent dopant may not be applicable or favorable for inspection of passive fibers or waveguides, but there is still a large group of active [2] and nonlinear [32] counterparts where the basic principle of our method can find its application. We believe that in general as long as a micro/nano waveguide is made of luminescent material, multimode interference at a suitable excitation wavelength in the waveguide could generate observable luminescence. Therefore, semiconductor nanowires and polymer fibers with luminescent dopants, for example, could be another platform where our approach also works. The luminescence mechanism can be single-photon spontaneous emission, nonlinear emitting process and so on. In [32] the authors had observed multimode interference pattern in CdSe nanowaveguides via third harmonic generation and multi-photon luminescence, implying various applicable scenarios of the presented method for different devices. The waveguide structure can also be used to investigate mode evolution under different propagation conditions such as sharp bending, scattering object attaching, structured waveguide surface and so on. Hence mode manipulation become possible once we know how the propagation is affected. Research of high order mode excitation at micro/nano scale can also be carried out on these platforms which offer direct indication of propagating modes. The approach demonstrated in our study may find wide applications on multimode nanophotonic circuits and devices.

Optics EXPRESS

Funding

National Natural Science Foundation of China (11527901); National Key Research and Development Project of China (2018YFB2200400).

Acknowledgments

The authors thank the Fundamental Research Funds for the Central Universities. The authors also thank Prof. Junjie Zhang from China Jiliang University for providing the Er^{3+}/Yb^{3+}-codoped tellurite glass generously. All data supporting this study are available from the University of Southampton repository at http://doi.org/10.5258/SOTON/D0995.

References

1. Y. Jeong, J. K. Sahu, D. N. Payne, and J. Nilsson, "Ytterbium-doped large-core fiber laser with 1.36 kW continuous-wave output power," Opt. Express **12**(25), 6088–6092 (2004).
2. D. J. Richardson, J. Nilsson, and W. A. Clarkson, "High power fiber lasers: current status and future perspectives [Invited]," J. Opt. Soc. Am. B **27**(11), B63–B92 (2010).
3. R. J. Mears, L. Reekie, I. M. Jauncey, and D. N. Payne, "Low-noise erbium-doped fibre amplifier operating at 1.54μm," Electron. Lett. **23**(19), 1026–1028 (1987).
4. R. Paschotta, J. Nilsson, A. C. Tropper, and D. C. Hanna, "Ytterbium-doped fiber amplifiers," IEEE J. Quantum Electron. **33**(7), 1049–1056 (1997).
5. L. Sun, S. Jiang, and J. R. Marciante, "All-fiber optical magnetic-field sensor based on Faraday rotation in highly terbium-doped fiber," Opt. Express **18**(6), 5407–5412 (2010).
6. S. Musolino, E. P. Schartner, G. Tsiminis, A. Salem, T. M. Monro, and M. R. Hutchinson, "Portable optical fiber probe for *in vivo* brain temperature measurements," Opt. Express **7**(8), 3069–3077 (2016).
7. T. Li, *Optical Fiber Communications: Fiber Fabrication* (Elsevier Science & Technology, 1985).
8. L. M. Tong, L. L. Hu, J. J. Zhang, J. R. Qiu, Q. Yang, J. Y. Lou, Y. H. Shen, J. L. He, and Z. Z. Ye, "Photonic nanowires directly drawn from bulk glasses," Opt. Express **14**(1), 82–87 (2006).
9. X. Q. Wu and L. M. Tong, "Optical microfibers and nanofibers," Nanophotonics **2**(5-6), 407–428 (2013).
10. X. S. Jiang, Q. Yang, G. Vienne, Y. H. Li, L. M. Tong, J. J. Zhang, and L. L. Hu, "Demonstration of microfiber knot laser," Appl. Phys. Lett. **89**(14), 143513 (2006).
11. W. Fan, J. L. Gan, Z. S. Zhang, X. M. Wei, S. H. Xu, and Z. M. Yang, "Narrow linewidth single frequency microfiber laser," Opt. Lett. **37**(20), 4323–4325 (2012).
12. W. Fan, Z. S. Zhang, J. L. Gan, X. M. Wei, H. C. Huang, S. H. Xu, and Z. M. Yang, "A wavelength tunable single frequency microfiber laser," Laser Phys. Lett. **11**(1), 015104 (2014).
13. M. C. Frawley, A. Petcu-Colan, V. G. Truong, and S. N. Chormaic, "Higher order mode propagation in an optical nanofiber," Opt. Commun. **285**(23), 4648–4654 (2012).
14. S. Ravets, J. E. Hoffman, L. A. Orozco, S. L. Rolston, G. Beadie, and F. K. Fatemi, "A low-loss photonic silica nanofiber for higher-order modes," Opt. Express **21**(15), 18325–18335 (2013).
15. F. Dubois, P. Emplit, and O. Hugon, "Selective mode excitation in graded-index multimode fiber by a computer-generated optical mask," Opt. Lett. **19**(7), 433–435 (1994).
16. G. Labroille, B. Denolle, P. Jian, P. Genevaux, N. Treps, and J. Morizur, "Efficient and mode selective spatial mode multiplexer based on multi-plane light conversion," Opt. Express **22**(13), 15599–15607 (2014).
17. A. Maimaiti, V. G. Truong, M. Sergides, I. Gusachenko, and S. N. Chormaic, "Higher order microfiber modes for dielectric particle trapping and propulsion," Sci. Rep. **5**(1), 9077 (2015).
18. A. Maimaiti, D. Holzmann, V. G. Truong, H. Ritsch, and S. N. Chormaic, "Nonlinear force dependence on optically bound micro-particle arrays in the evanescent fields of fundamental and higher order microfibre modes," Sci. Rep. **6**(1), 30131 (2016).
19. Y. P. Huang, F. Shi, T. Wang, X. M. Liu, X. L. Zeng, F. F. Pang, T. Y. Wang, and P. Zhou, "High-order mode Yb-doped fiber lasers based on mode-selective couplers," Opt. Express **26**(15), 19171–19181 (2018).
20. Y. M. Zhang, H. X. Li, C. S. Dai, L. X. Xu, C. Gu, W. Chen, Y. G. Zhu, P. J. Yao, and Q. W. Zhan, "All-fiber high-order mode laser using a metal-clad transverse mode filter," Opt. Express **26**(23), 29679–29686 (2018).
21. S. Ramachandran and P. Kristensen, "Optical vortices in fiber," Nanophotonics **2**(5-6), 455–474 (2013).
22. J. Wang, "Advances in communications using optical vortices," Photonics Res. **4**(5), B14–B28 (2016).
23. K. Foubert, L. Lalouat, B. Cluzel, E. Picard, D. Peyrade, E. Delamadeleine, F. de Fornel, and E. Hadji, "Near-field modal microscopy of subwavelength light confinement in multimode silicon slot waveguides," Appl. Phys. Lett. **93**(25), 251103 (2008).
24. M. Szczurowski, W. Urbanczyk, M. Napiorkowski, P. Hlubina, U. Hollenbach, H. Sieber, and J. Mohr, "Differential Rayleigh scattering method for measurement of polarization and intermodal beat length in optical waveguides and fibers," Appl. Opt. **50**(17), 2594–2600 (2011).
25. J. E. Hoffman, F. K. Fatemi, G. Beadie, S. L. Rolstion, and L. A. Orozco, "Rayleigh scattering in an optical nanofiber as a probe of higher-order mode propagation," Optica **2**(5), 416–423 (2015).

Optics EXPRESS

26. G. P. Agrawal, *Fiber-optic Communication Systems* (Wiley, 2010), Chap. 2.
27. J. P. Wittke, I. Ladany, and P. N. Yocom, "Y_2O_3 : Yb : Er-New Red-Emitting Infrared-Excited Phosphor," J. Appl. Phys. **43**(2), 595–600 (1972).
28. K. Z. Zheng, D. Zhao, D. S. Zhang, N. Liu, and W. P. Qin, "Ultraviolet upconversion fluorescence of Er^{3+} induced by 1560 nm laser excitation," Opt. Lett. **35**(14), 2442–2444 (2010).
29. G. Y. Chen, T. Y. Ohulchanskyy, A. Kachynski, H. Ågren, and P. N. Prasad, "Intense Visible and Near-Infrared Upconversion Photoluminescence in Colloidal LiYF4:Er3+ Nanocrystals under Excitation at 1490 nm," ACS Nano **5**(6), 4981–4986 (2011).
30. C. D. Poole, J. M. Wiesenfeld, and A. R. McCormick, "Broadband dispersion compensation by using the higher-order spatial mode in a two-mode fiber," Opt. Lett. **17**(14), 985–987 (1992).
31. H. Nyquist, "Certain topics in telegraph transmission theory," Proc. IEEE **90**(2), 280–305 (2002).
32. J. X. Yu, F. Liu, Z. Q. Gu, F. X. Gu, and S. L. Zhuang, "Efficient higher-order nonlinear optical effects in CdSe nanowaveguides," Opt. Express **26**(6), 6880–6889 (2018).